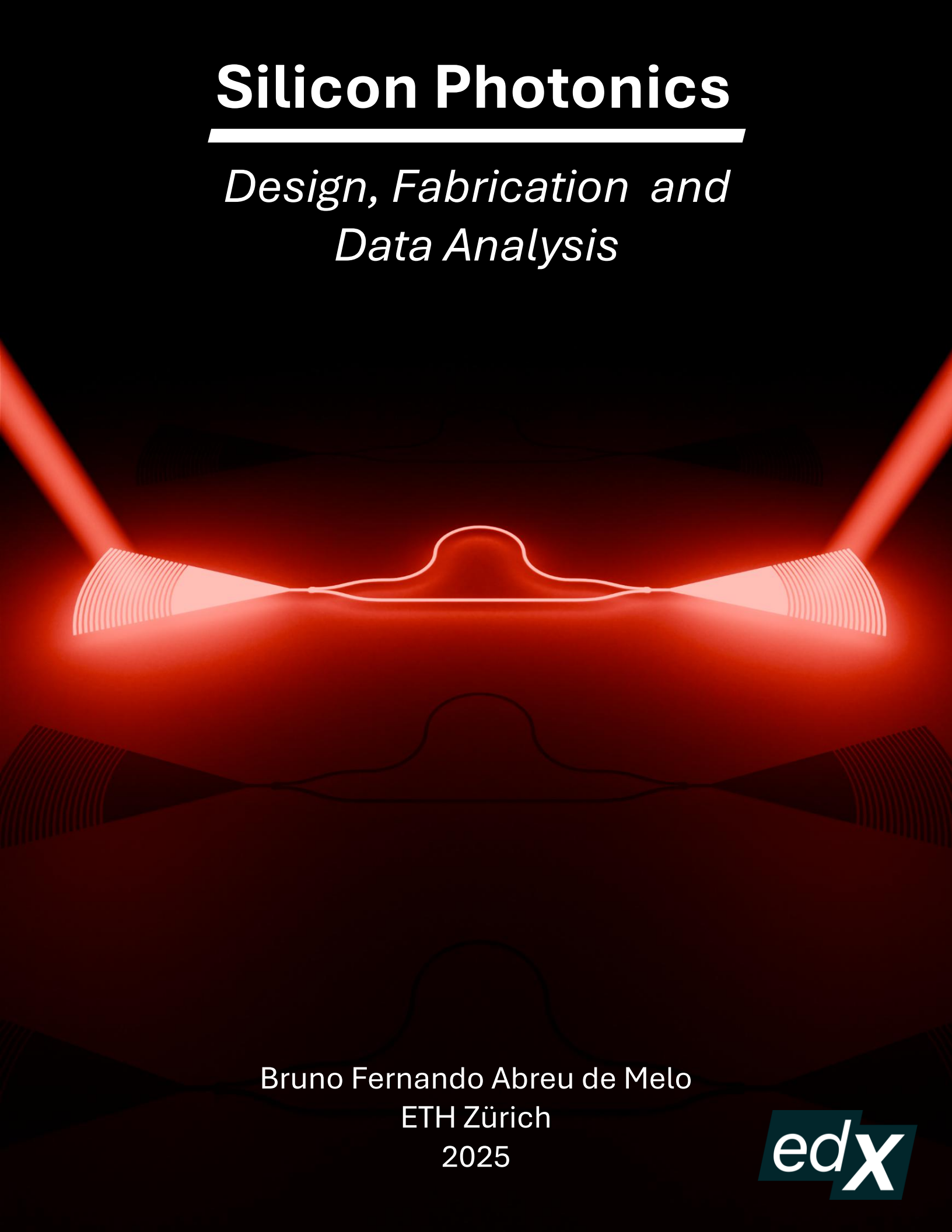


Silicon Photonics

*Design, Fabrication and
Data Analysis*

The background of the slide features a stylized, abstract representation of light propagation in a silicon photonic waveguide. It consists of several parallel, wavy lines of varying shades of red and orange, set against a dark background. These lines represent the path of light as it travels through a waveguide, with some lines appearing brighter and others darker, suggesting intensity or depth.

Bruno Fernando Abreu de Melo
ETH Zürich
2025



Design of an integrated Mach Zehnder interferometer

Bruno Fernando Abreu de Melo (bruno_b_fernando_f)

I. INTRODUCTION

THE Mach–Zehnder interferometer (MZI) is a powerful optical device used to study the interference of light waves and their behavior under different conditions [1]. It works by splitting a single beam of light into two separate paths, allowing them to travel independently before being recombined. When the beams meet again, differences in their paths—such as variations in distance, refractive index, or phase—produce an interference pattern. This pattern provides valuable information about the properties of the light and the medium through which it has traveled.

Because of its versatility, the Mach–Zehnder interferometer is widely used in physics and engineering research. It serves as a tool for exploring fundamental concepts in wave optics, as well as for practical applications like sensing, communications, and precision measurements. Its design is conceptually straightforward yet highly adaptable, making it a common choice for experiments that require controlled interference of light.

II. THEORY

We implement MZIs using silicon photonic integrated circuits [2], [3], as shown in Fig. 1. Light at a wavelength λ_0 is coupled into the circuit through a grating coupler and split into two waveguides of lengths L_1 and L_2 by a Y-junction. The two beams are recombined by a second Y-junction, and a grating coupler sends the light into an optical fiber for measuring the interference power. Here we derive the expression for the transmission spectrum of the MZI as a function of the waveguides properties and the path lengths L_1 and L_2 .

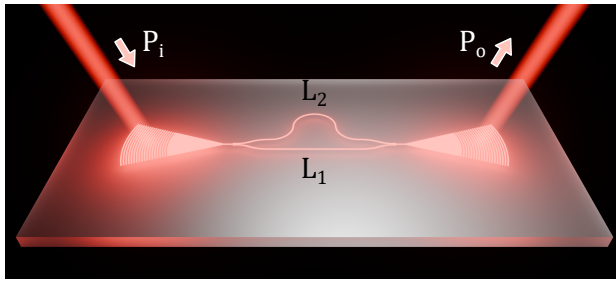


Fig. 1. **Schematic of an integrated MZI.** A laser beam of power P_i and wavelength λ_0 is coupled into the circuit through a grating coupler and split into two waveguides of lengths L_1 and L_2 by a Y-junction. The two beams are recombined by a second Y-junction, and a grating coupler sends the light into an optical fiber for measuring the interference power.

The propagation speed of a continuous wave in a waveguide is characterized by the effective refractive index

$$n_{\text{eff}}(\lambda_0) = \frac{\beta(\lambda_0)\lambda_0}{2\pi} \quad (1)$$

where $\beta(\lambda_0)$ is the propagation constant, similar to the wavenumber $k = 2\pi n/\lambda$ for a wave propagating in a medium of refractive index n . The value of $n_{\text{eff}}(\lambda)$ depends on the geometry of the waveguide and its material properties.

On the other hand, the propagation speed of pulses in the waveguide is dictated by the group refractive index

$$n_g(\lambda_0) = n_{\text{eff}}(\lambda_0) - \lambda_0 \left. \frac{dn_{\text{eff}}(\lambda)}{d\lambda} \right|_{\lambda=\lambda_0} \quad (2)$$

For simplicity, we assume $n_{\text{eff}}(\lambda)$ to be identical in all waveguides in the circuit, such that the intensity at the output of the MZI is given by

$$I_o = \frac{I_i}{2}(1 + \cos(\beta(\lambda_0)\Delta L)) \quad (3)$$

where $\Delta L = L_2 - L_1$, leading to a transfer function

$$T(\lambda) = \frac{1 + \cos(\beta(\lambda)\Delta L)}{2} \quad (4)$$

Note that this transfer function assumes no losses. In practice, wavelength-dependent losses are present in all components of the circuit [4], affecting the real value of $T(\lambda)$.

The intensity I_o is maximum when $\beta(\lambda_0)\Delta L = 2m\pi$, with $m \in \mathbb{Z}$. The difference $\Delta\lambda$ between two consecutive values of λ_0 satisfying this relation is called the free spectral range (FSR). The difference between the corresponding values of β is

$$\Delta\beta = -\frac{2\pi}{\Delta L}, \quad (5)$$

which can also be written using Eq. 1 as

$$\Delta\beta = \frac{2\pi}{\lambda_0 + \Delta\lambda} n_{\text{eff}}(\lambda_0 + \Delta\lambda) - \frac{2\pi}{\lambda_0} n_{\text{eff}}(\lambda_0) \quad (6)$$

Expanding Eq. 6 for $\Delta\lambda \ll \lambda_0$ and approximating

$$n_{\text{eff}}(\lambda_0 + \Delta\lambda) \approx n_{\text{eff}}(\lambda_0) + \Delta\lambda \left. \left(\frac{dn_{\text{eff}}}{d\lambda} \right) \right|_{\lambda=\lambda_0} \quad (7)$$

gives:

$$\begin{aligned} \Delta\beta &= -\frac{2\pi\Delta\lambda}{\lambda_0^2} \left(n_{\text{eff}}(\lambda_0) - \lambda_0 \left. \frac{dn_{\text{eff}}}{d\lambda} \right|_{\lambda=\lambda_0} \right) \\ &= -\frac{2\pi\Delta\lambda}{\lambda_0^2} n_g(\lambda_0) \end{aligned} \quad (8)$$

Putting together Eqs. 5 and 8, we find that the FSR is given by

$$\Delta\lambda = \frac{\lambda_0^2}{n_g(\lambda_0)\Delta L} \quad (9)$$

III. WAVEGUIDE SIMULATIONS

In our integrated MZI we use strip silicon waveguides ($n \approx 3.48$) with a silica cladding ($n \approx 1.44$). The height of the waveguide is set to $h = 220$ nm, which is the standard silicon layer thickness in the CMOS industry, while the width is set to $w = 500$ nm. We use Lumerical FDE (Ansys, Inc.) to simulate the electric field corresponding to the transverse electrical (TE) and transverse magnetical (TM) modes of the waveguide. The TE mode, shown in Fig. 2(a), is more confined inside the waveguide than the TM mode, shown in Fig. 2(b).

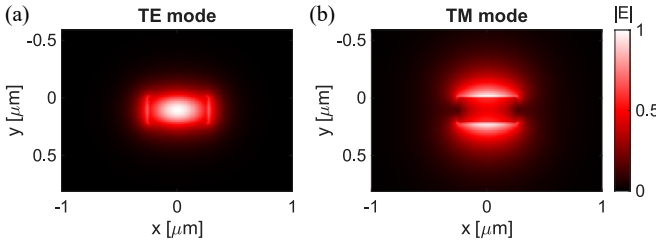


Fig. 2. **Eigenmodes of the waveguide.** (a) TE mode. (b) TM mode. We use a simulation region of $3\text{ }\mu\text{m} \times 2\text{ }\mu\text{m}$. The wavelength is $\lambda_0 = 1550$ nm.

We scan the wavelength over $1450\text{ nm} \leq \lambda \leq 1750\text{ nm}$ to obtain $n_{\text{eff}}(\lambda)$, shown in Fig. 3(a) for the TE (red points) and TM modes (gray points). We fit $n_{\text{eff}}(\lambda)$ to

$$n_{\text{eff}}(\lambda) = n_1 + n_2(\lambda - \lambda_0) + n_3(\lambda - \lambda_0)^2 \quad (10)$$

with $\lambda_0 = 1550$ nm to obtain the compact waveguide model (solid lines in Fig. 3(a)). The fitted parameters for the TE mode and the TM mode are $(n_1, n_2, n_3) = (2.45, -1.13\text{ }\mu\text{m}^{-1}, -0.04\text{ }\mu\text{m}^{-2})$ and $(n_1, n_2, n_3) = (1.77, -1.27\text{ }\mu\text{m}^{-1}, 1.81\text{ }\mu\text{m}^{-2})$.

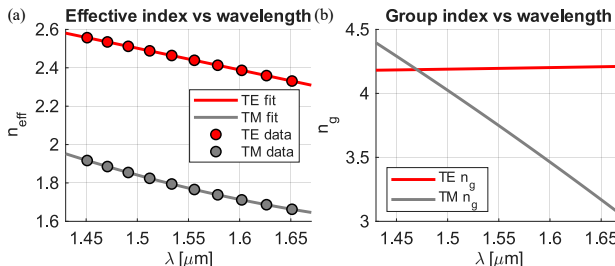


Fig. 3. **Refractive indices in the waveguide.** (a) Effective refractive index n_{eff} as a function of λ obtained from the simulation of the waveguide TE (red points) and TM (gray points) modes. We fit n_{eff} to a polynomial model (dashed curves) to obtain the waveguide compact model. (b) Group refractive index n_g obtained from the waveguide compact model.

From the waveguide compact model we can obtain the derivative of $n_{\text{eff}}(\lambda)$:

$$\frac{dn_{\text{eff}}}{d\lambda} = n_2 + 2n_3(\lambda - \lambda_0). \quad (11)$$

Using Eq. 2, we can then calculate the group index:

$$n_g(\lambda) = n_{\text{eff}}(\lambda) - \lambda(n_2 + 2n_3(\lambda - \lambda_0)) \quad (12)$$

Fig. 3(b) shows the group index n_g as a function of λ for the TE (red) and TM (gray) modes. While the group refractive index is approximately constant for the TE mode, it varies

significantly for the TM mode. At the center wavelength $\lambda_0 = 1550$ nm we have $n_g \approx 4.20$ for the TE mode and $n_g \approx 3.75$ for the TM mode.

The group index n_g can be used to calculate the FSR of the MZI using Eq. 9. We plot $\Delta\lambda$ as a function of ΔL in Fig. 4 for the TE (red) and TM (gray) modes. Because n_g is smaller for the TM mode, $\Delta\lambda$ is smaller for the TE mode for a given ΔL .

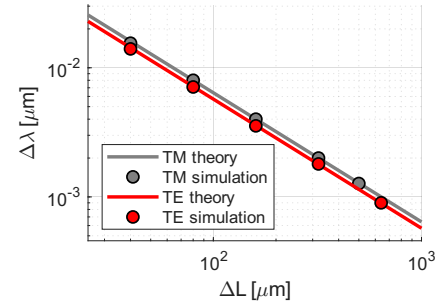


Fig. 4. **Free spectral range of the MZI.** FSR as a function of the path length difference ΔL for the TE (red) and TM (gray) modes calculated using the value of n_g extracted from the waveguide compact model (solid line) and extracted from the circuit simulation (points).

We simulate the MZI interferometer using Lumerical Interconnect (Ansys, Inc.), as shown in Fig 5(a), for different values of ΔL . We use components from the SiEPIC library, to capture the wavelength dependent losses of and efficiencies of real devices. In Fig 5(b) we show the transfer function of the simulated TE (solid red) and TM modes (solid gray) for $\Delta L = 40\text{ }\mu\text{m}$. The maximum transmission is around -5 dB, and it decays as the wavelength moves away from 1550 nm. The FSR is approximately 13.9 nm for the TE mode, and 15.5 nm for TM. The FSR obtained from simulating circuits with different ΔL for both modes is shown as points in Fig 4. For our MZI design, we use the path length differences shown in Table I.

TE mode		TM mode	
ΔL [μm]	$\Delta\lambda$ [nm]	ΔL [μm]	$\Delta\lambda$ [nm]
40	14.3	40	16.02
80	7.15	80	8.01
160	3.58	160	4.00
320	1.79	320	2.00
640	0.89	500	1.28

TABLE I
EXPECTED FSR FOR DIFFERENT PATH LENGTH DIFFERENCES ΔL . THE VALUE OF $\Delta\lambda$ IS CALCULATED USING EQ. 9 AND THE GROUP INDICES n_g OBTAINED FROM THE WAVEGUIDE COMPACT MODEL.

IV. FABRICATION

The devices are fabricated on a silicon-on-insulator wafer with a buried oxide thickness of $2\text{ }\mu\text{m}$ and a 220 nm silicon top layer (see Fig 6). The wafer is first spin-coated with the negative resist hydrogen silsesquioxane (HSQ) at 4000 rpm and baked at 80°C for 4 min. The resist is then patterned using electron-beam lithography (EBL, JEOL JBX-6300FS) and developed by immersion in 25% tetramethylammonium hydroxide (TMAH) for 4 min. The silicon is subsequently

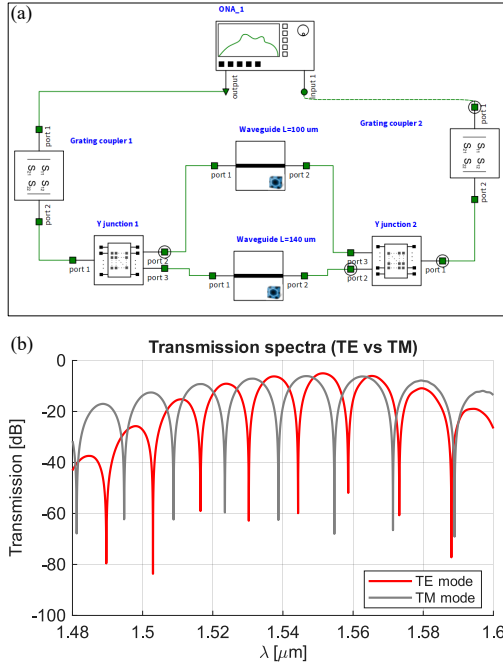


Fig. 5. **Simulated transmission spectra of an MZI.** (a) Layout in Lumerical Interconnect used to simulate the transmission spectrum. (b) Transmission spectra for an MZI with $\Delta L = 40 \mu\text{m}$ using TE (red) and TM (gray) light.

etched using inductively coupled plasma (ICP, Oxford Plasmalab System 100) with a chlorine flow of 20 sccm, a chamber pressure of 20 mT, an ICP power of 800 W, a bias power of 40 W, a bias voltage of 185 V, and a platen temperature of 20 °C. After stripping the HSQ, an oxide cladding with a thickness of 2–3 μm is deposited using plasma-enhanced chemical vapor deposition (PECVD).

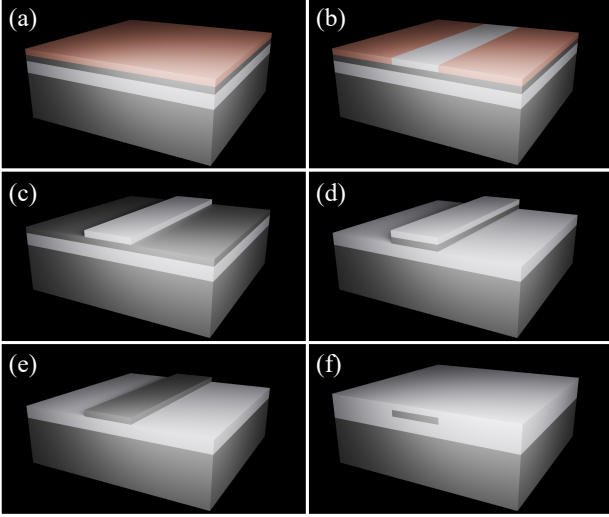


Fig. 6. **Fabrication.** (a) Spin coating with HSQ. (b) Resist exposure with EBL. (c) HSQ development. (d) Etching with ICP. (e) HSQ stripping. (f) Cladding deposition with PECVD.

Fig 7 shows the designed (left) and fabricated (right) MZIs. The bending radius can be much smaller when using TE polarization ($R = 5 \mu\text{m}$, Fig 7(a)) than when using TM polarization

($R = 15 \mu\text{m}$, Fig 7(b)) due to the larger confinement of the TE mode.

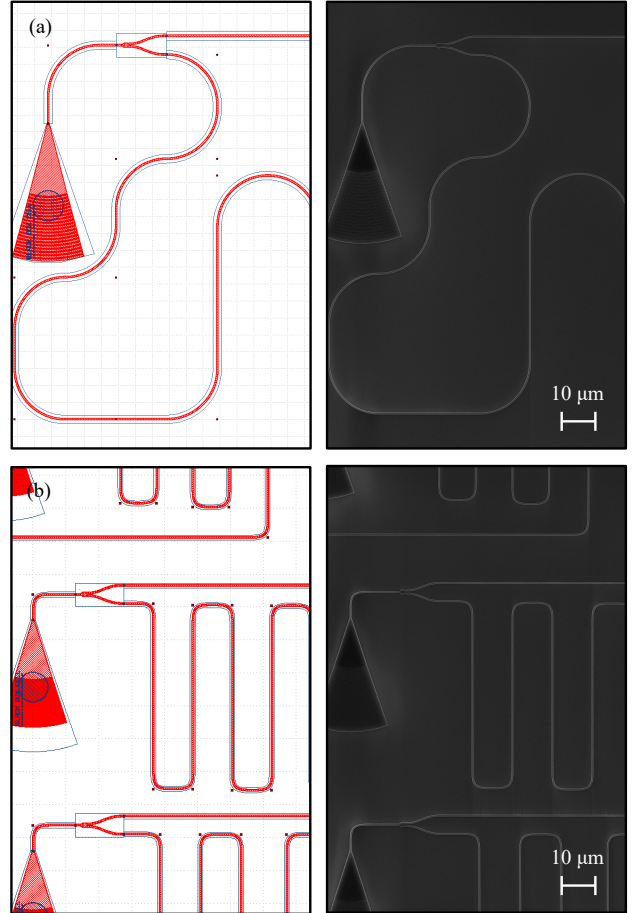


Fig. 7. **Comparison between designed and fabricated MZIs** (a) TM mode and (b) TE mode MZIs. The figures on the left show the design in KLayout, while the figures on the right show the pictures of the fabricated devices taken with a scanning electron microscope (SEM).

A. Fabrication variability and corner analysis

The waveguides are designed with nominal dimensions of $w_0 = 500 \text{ nm}$ and $h_0 = 220 \text{ nm}$. In practice, the fabricated dimensions can deviate noticeably from these targets. Variations in the waveguide height arise from non-uniformity in the silicon layer thickness across the SOI chip, while variations in width are introduced by differences in the resist properties, resist exposure and development, and the etching process. For the fabrication process considered in this report, the measured extremes are $h_{\min} = 215.3 \text{ nm}$, $h_{\max} = 223.1 \text{ nm}$, $w_{\min} = 470 \text{ nm}$, and $w_{\max} = 470 \text{ nm}$.

These dimensional variations lead to corresponding variations in the group index n_g , which in turn affect both the FSR $\Delta\lambda$ and the center wavelength of the MZI. To determine $n_{g,\min}$ and $n_{g,\max}$, we evaluate the group index at the corners of the parameter space defined by the expected dimensional ranges, as illustrated in Fig. 8, using Lumerical MODE.

Fig 9 shows the effective index n_{eff} and the group index n_g as a function of the wavelength λ for the TE and TM modes.

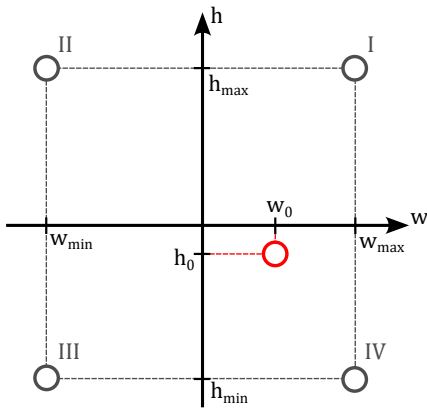


Fig. 8. **Corner analysis.** The waveguide is designed with width w_0 and height h_0 . Due to the fabrication process, the actual width can vary from w_{\min} to w_{\max} , and the height from h_{\min} to h_{\max} .

The values of n_g for the TE and TM modes for a wavelength $\lambda_0 = 1550$ nm are listed in Table IV-A.

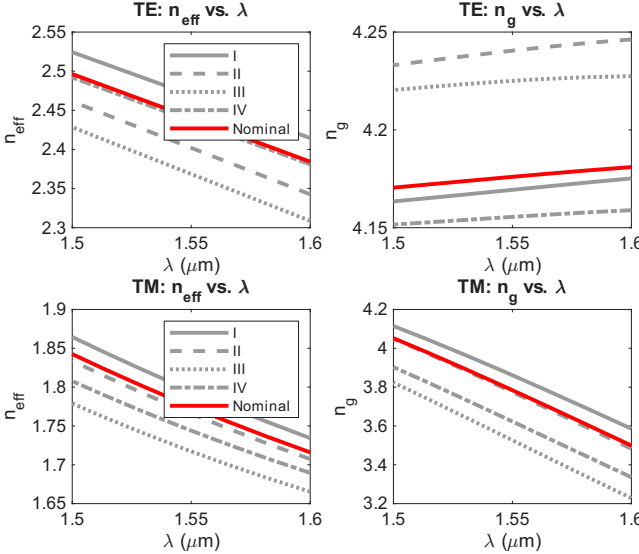


Fig. 9. **Refractive index variation due to fabrication variability.** Effective index n_{eff} (left) and group index n_g (right) for the TE (top) and TM (bottom) modes. The curve for the nominal design parameters (red curves) lie between the curves for the corners of the parameters space illustrated in Fig 8 (gray curves).

Point	n_g^{TE}	n_g^{TM}
I	4.1702	3.8236
II	4.2414	3.7342
III	4.2256	3.4840
IV	4.1561	3.5826
Nominal	4.1756	3.8027

TABLE II

GROUP INDEX FOR THE FOUR CORNER POINTS AND THE NOMINAL DESIGN DIMENSIONS SHOWS IN FIG 8.

From the maximum and minimum values of n_g , we can determine how much $\Delta\lambda$ may deviate from its nominal value. For the TE mode, $\Delta\lambda$ can be roughly 1% smaller or larger than the nominal value, while for the TM mode it can be about 2% smaller or up to 4% larger. Additionally, the variability in

n_{eff} leads to a variation in the position of the minima in the transmission spectra. This is seen in Fig 10, where $T(\lambda)$ is shown for the different points of the corner analysis for the TE (red) and TM (gray) modes.

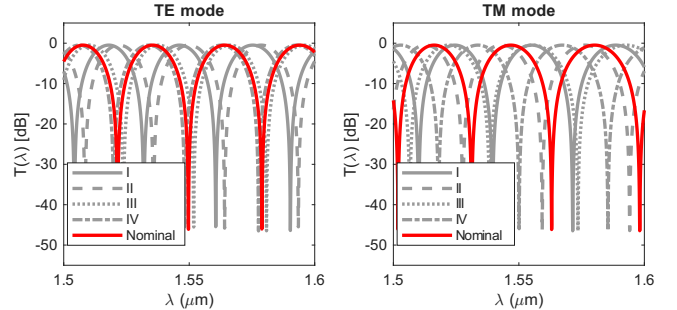


Fig. 10. **Transmission spectra for different points of the corner analysis.** The variation in n_{eff} leads to variation in the positions of the minimum of $T(\lambda)$ relative to the nominal spectrum (red curves) both for the TE (left) and the TM (right) modes.

V. DEVICE CHARACTERIZATION AND DATA ANALYSIS

The transmission $T(\lambda)$ of the fabricated MZIs is measured for wavelengths ranging from 1475 nm to 1580 nm. The efficiency of the grating couplers used to couple light into the device is wavelength dependent, as seen in the transmission spectrum of the loopback structure in Fig 11(a) for the TE mode. We therefore analyze only the data in the range $1500 \text{ nm} \leq \lambda \leq 1570 \text{ nm}$, since the coupling efficiency of the TE gratings is too low outside of this range. For the TM mode, the coupling efficiency is sufficiently large over the whole measurement range.

To remove the wavelength dependence of the grating couplers from the measured spectrum, we divide $T(\lambda)$ of the MZI, shown in Fig 11(b), by $T(\lambda)$ of the calibration structure. As shown in Fig 11(c), the envelope given by the grating spectrum is no longer present in the resulting $T(\lambda)$.

The calibrated $T(\lambda)$ in logarithmic units is fitted to

$$T(\lambda) = 10 \log_{10} \left(\frac{1}{4} |1 + \exp(-i\beta(\lambda)\Delta L - \alpha\Delta L/2)|^2 \right) + b \quad (13)$$

where α is the waveguide loss, b is the insertion loss and $\beta(\lambda)$ is given by Eq 1. The fit parameters are b and n_1, n_2, n_3 defined in Eq 10. In Fig 12(a), the fitted curve (dotted gray) shows reasonable agreement with the calibrated spectrum (red) of the TE MZI with $\Delta L = 40 \mu\text{m}$. While there is good agreement regarding the position of the minimum at $\lambda \approx 1525 \text{ nm}$, the fit does not capture well the position of the other minima.

From the fitted parameters, we calculate the effective index $n_{\text{eff}}(\lambda)$ using Eq 10 and the group index $n_g(\lambda)$ using Eq 12. Fig 12(b) shows the measured indices n_{eff} (gray) and n_g (red) for the TE MZI with $\Delta L = 40 \mu\text{m}$. As expected from the plots in Fig 9, n_{eff} decreases with increasing λ , while n_g increases.

We compare the measured indices from each MZI (Fig 13) with the range of values expected from the corner analysis (shaded region). The measured curves fall within the expected regions for all devices, with the exception of the TE MZI with

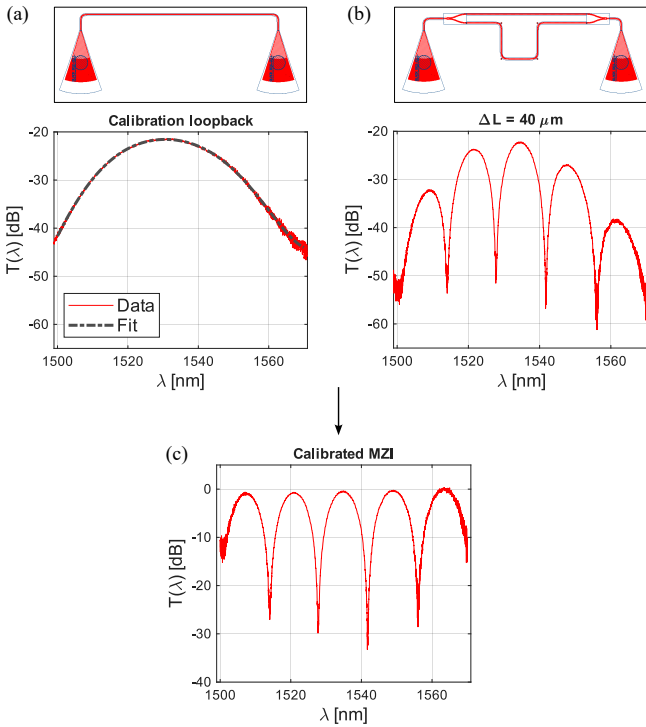


Fig. 11. Calibration with a loopback structure. (a) Spectrum of a loopback structure consisting of two grating couplers connected by a waveguide. (b) Spectrum of the MZI with $\Delta L = 40 \mu\text{m}$. (c) Calibrated spectrum obtained by dividing the MZI spectrum by the loopback spectrum.

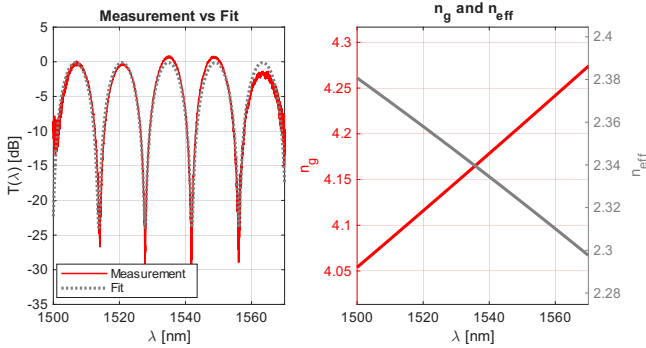


Fig. 12. Fit of the measured spectrum (a) Calibrated spectrum (red) and fit to the theoretical model (dotted gray). (b) Indices n_{eff} (gray) and n_g (red) extracted from the fit.

$\Delta L = 40 \mu\text{m}$. This might be due to the slight disagreement between the position of the minima in the measurement and the fit in Fig 12(a), or due to deviations in the geometry of the structure occurring during the fabrication process.

Finally, we use the measured n_g to calculate the FSR at $\lambda = 1550 \text{ nm}$. Fig 14(a) shows $\Delta\lambda$ as a function of ΔL for the fabricated devices (points), which show good agreement to the curves calculated from the compact model of the waveguide. Fig 14(b) shows the deviation of the measured values of $\Delta\lambda$ from the ones expected from the waveguide compact model, which remains below 1%.

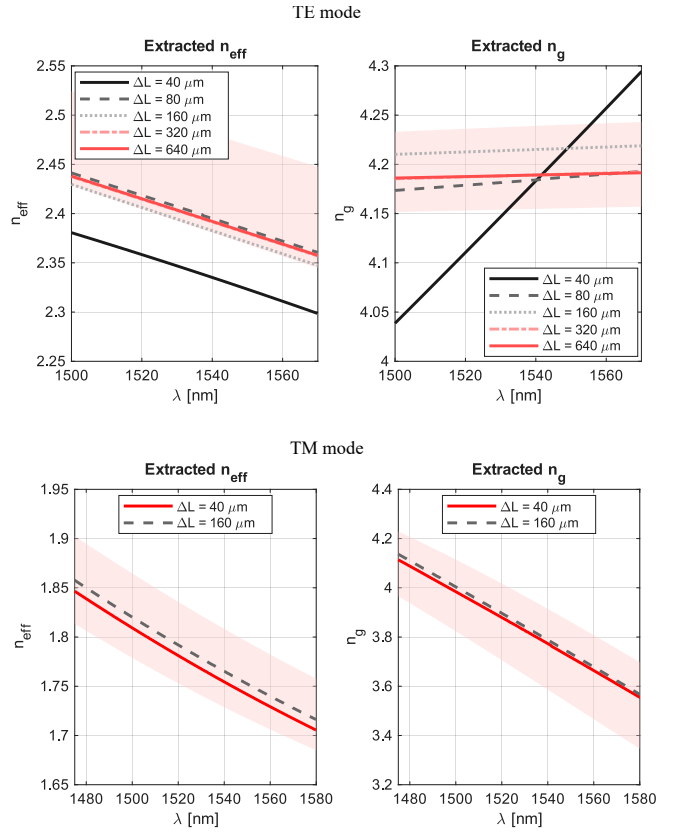


Fig. 13. Refractive indices extracted from different MZIs. Indices n_{eff} (left) and n_g (right) extracted from TE (top) and TM (bottom) MZIs with different path length differences. The shaded region corresponds to the range of values resulting from the corner analysis. Note that the data for the TM MZIs with $\Delta L = 80, 320, 500 \mu\text{m}$ was not available.

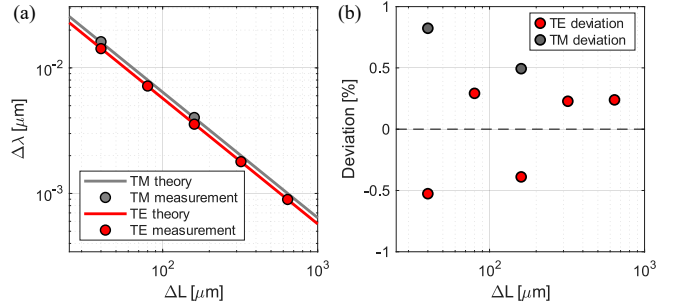


Fig. 14. Free spectral range of the fabricated MZIs. (a) FSR as a function of the path length difference ΔL for the TE (red) and TM (gray) modes calculated using the value of n_g extracted from the waveguide compact model (solid line) and extracted from the fit of the measured transmission spectra (points). (b) Deviation of the measured values of $\Delta\lambda$ from the ones expected from the waveguide compact model.

VI. EFFECTIVE INDEX TUNING WITH SUB-WAVELENGTH GRATINGS

A. Theory

In the previous designs we considered MZIs in which the FSR could be controlled by changing the path length difference between the arms. We now consider MZIs with a fixed path length difference, and change the FSR by tuning the refractive index of the waveguides.

The refractive index can be tuned by using subwavelength grating (SWG) waveguides [5], [6]. SWG waveguides consists of pillars arranged with periodicity $\Lambda \ll \lambda$, as shown in Fig 15. When this condition is satisfied, light propagates without diffracting as in standard gratings with $\Lambda \approx \lambda$. Instead, the structure behaves as a medium with a refractive index $n(DC)$, where $DC = \ell/\Lambda$ is the duty cycle, with ℓ being the length of a grating pillar. By tuning DC , one can tune n_g .

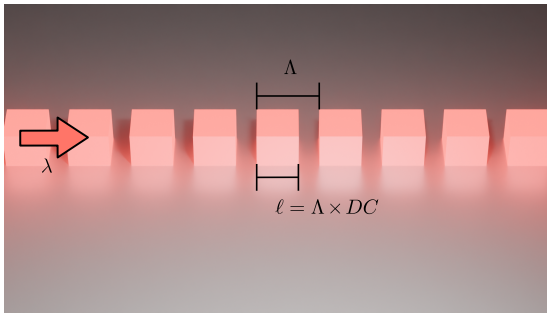


Fig. 15. **Sub-wavelength grating.** The waveguide is formed by rectangular pillars positioned with periodicity $\Lambda \ll \lambda$. The duty cycle DC is defined as $DC = \ell/\Lambda$.

B. Design

We design our MZI with $\Delta L = 100 \mu\text{m}$, as shown in Fig 16. Both arms contain two SWG waveguides and the same number of bends, such that the phase difference is given by:

$$\Delta\phi = \beta(\lambda, DC)\Delta L \quad (14)$$

where $\beta(\lambda, DC) = 2\pi n_{\text{eff}}(\lambda, DC)/\lambda$. We choose a periodicity $\Lambda = 200 \text{ nm}$ while keeping $w = 500 \text{ nm}$ and $h = 220 \text{ nm}$. To keep a margin from the resolution of the fabrication process, we vary DC from 0.3, corresponding to pillars of length $\ell = \Lambda \times DC = 60 \text{ nm}$, to 0.8, corresponding to gaps of length $\Lambda - \ell = (1 - DC)\Lambda = 40 \text{ nm}$. We also fabricate one device with $DC = 1$, corresponding to a conventional single mode waveguide.

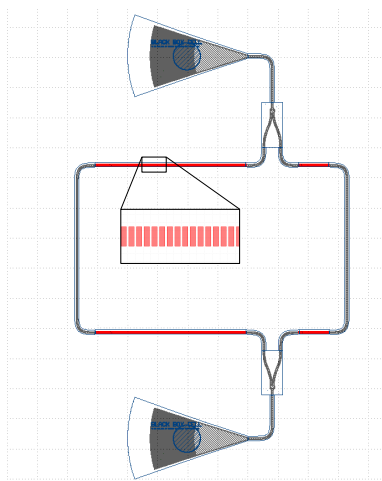


Fig. 16. **Design of an MZI with SWG waveguides.** Both arms of the MZI contain two segments of SWG waveguides (red), but with different lengths, resulting in $\Delta L = 100 \mu\text{m}$. Inset: SWG with $\Lambda = 200 \text{ nm}$ and $DC = 0.7$.

C. Device characterization

We use the same fitting procedures described for the conventional MZIs to calibrate the measured spectra and to extract the group index n_g for the different duty cycles DC . The group index n_g increases with increasing DC , as seen in Fig 17. The behavior is mostly linear, with an outlier at $DC = 0.8$. The spectra for $DC < 0.4$ could not be fitted due to the high losses introduced by the SWG waveguides. Since the effective index of the conventional and SWG waveguides is different, the transition between one type of waveguide to the other introduces significant losses.

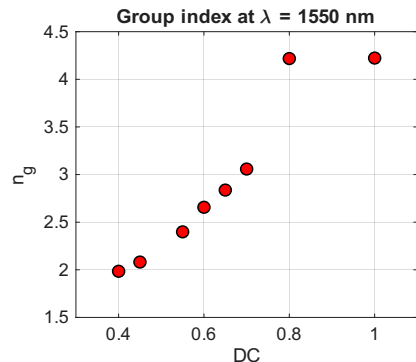


Fig. 17. **Refractive index tuning in a sub-wavelength grating waveguide.** Group index v_g as a function of the duty cycle DC . The path length difference is $\Delta L = 100 \mu\text{m}$ and the mode is TE polarized.

VII. CONCLUSIONS

This work presented the complete design, simulation, fabrication, and characterization of integrated Mach-Zehnder interferometers on a silicon photonics platform. Beginning with the theoretical description of interference and guided-wave propagation, we used numerical mode solvers to extract effective and group indices for both TE and TM modes, enabling accurate predictions of the free spectral range for different path-length imbalances. Circuit-level simulations confirmed these trends and guided the selection of device geometries.

Fabricated devices demonstrated good agreement with theoretical and simulated behavior, with measured refractive indices and FSR values mostly falling within the bounds predicted by the corner analysis. Deviations observed in one structure highlight the sensitivity of silicon photonic circuits to dimensional variations introduced during lithography and etching.

Finally, we explored refractive-index engineering using subwavelength grating waveguides, showing that the group index can be tuned by adjusting the duty cycle. This approach enables controlling the spectral response of interferometric devices without modifying their physical footprint.

Overall, the results validate both the robustness and versatility of silicon photonics for integrated interferometric devices, while illustrating the importance of accurate modeling, fabrication-aware design, and systematic characterization.

ACKNOWLEDGMENTS

We acknowledge the edX UBCx Phot1x Silicon Photonics Design, Fabrication and Data Analysis course, which is supported by the Natural Sciences and Engineering Research Council of Canada (NSERC) Silicon Electronic-Photonic Integrated Circuits (SiEPIC) Program. The devices were fabricated by Richard Bojko at the University of Washington Washington Nanofabrication Facility, part of the National Science Foundation's National Nanotechnology Infrastructure Network (NNIN), and Cameron Horvath at Applied Nanotools, Inc. Omid Esmaeeli performed the measurements at The University of British Columbia. We acknowledge Lumerical Solutions, Inc., Mathworks, Mentor Graphics, Python, and KLayout for the design software.

REFERENCES

- [1] A. Saleh and M. C. Teich, *Fundamentals of Photonics*, Aug 1991. [Online]. Available: <https://onlinelibrary.wiley.com/doi/10.1002/0471213748#aboutBook-pane>
- [2] S. A. Miller, M. Yu, X. Ji, A. G. Griffith, J. Cardenas, A. L. Gaeta, and M. Lipson, "Low-loss silicon platform for broadband mid-infrared photonics," *Optica*, vol. 4, no. 7, p. 707–707, Jun 2017. [Online]. Available: <https://opg.optica.org/optica/fulltext.cfm?uri=optica-4-7-707>
- [3] L. Chrostowski and M. Hochberg, *Silicon Photonics Design*. Cambridge University Press, Feb 2015. [Online]. Available: <https://www.cambridge.org/core/books/silicon-photonics-design/BF3CF13E8542BCE67FD2BBC7104ECEAB>
- [4] Y. A. Vlasov and S. J. McNab, "Losses in single-mode silicon-on-insulator strip waveguides and bends," *Optics Express*, vol. 12, no. 8, p. 1622, 2004. [Online]. Available: <https://opg.optica.org/oe/fulltext.cfm?uri=oe-12-8-1622>
- [5] P. J. Bock, P. Cheben, J. H. Schmid, J. Lapointe, A. Delâge, S. Janz, G. C. Aers, D.-X. Xu, A. Densmore, and T. J. Hall, "Subwavelength grating periodic structures in silicon-on-insulator: a new type of microphotonic waveguide," *Opt. Express*, vol. 18, no. 19, pp. 20 251–20 262, Sep 2010. [Online]. Available: <https://opg.optica.org/oe/abstract.cfm?URI=oe-18-19-20251>
- [6] P. Cheben, P. J. Bock, J. H. Schmid, J. Lapointe, S. Janz, D.-X. Xu, A. Densmore, A. Delâge, B. Lamontagne, and T. J. Hall, "Refractive index engineering with subwavelength gratings for efficient microphotonic couplers and planar waveguide multiplexers," *Opt. Lett.*, vol. 35, no. 15, pp. 2526–2528, Aug 2010. [Online]. Available: <https://opg.optica.org/ol/abstract.cfm?URI=ol-35-15-2526>